ACS APPLIED MATERIALS & INTERFACES

Research Article

Cite This: ACS Appl. Mater. Interfaces 2019, 11, 13608−13615

www.acsami.org

Bioinspired Hairy Skin Electronics for Detecting the Direction and Incident Angle of Airflow

Sungwoo Chun,[†] Wonkyeong Son,[‡] Changsoon Choi,[‡] Hyeongho Min,[†] Jiwon Kim,[§] Heon Joon Lee,[§] Dongjin Kim,[∥] Changhwan Kim,[∥] Je-sung Koh,[∥] and Changhyun Pang*,[†,§]

[†]Department of SKKU Advanced Institute of Nanotechnology (SAINT) and [§]School of Chemical Engineering, Sungkyunkwan University, Suwon, Gyeonggi-do 16419, Republic of Korea

[‡]Department of Smart Textile Convergence Research, Daegu Gyeongbuk Institute of Science and Technology (DGIST), Daegu 42988, Republic of Korea

[∥]Department of Mechanical Engineering, Ajou University, Suwon, Gyeonggi-do 16499, Republic of Korea

Supporting Information

ABSTRACT: The human skin has inspired multimodal detection using smart devices or systems in fields including biomedical engineering, robotics, and artificial intelligence. Hairs of a high aspect ratio (AR) connected to follicles, in particular, detect subtle structural displacements by airflow or ultralight touch above the skin. Here, hairy skin electronics assembled with an array of graphene sensors (16 pixels) and artificial microhairs for multimodal detection of tactile stimuli and details of airflows (e.g., intensity, direction, and incident angle) are presented. Composed of percolation networks of graphene nanoplatelet sheets, the sensor array can simultaneously detect pressure, temperature, and vibration, all of which correspond to the sensing range of human tactile perceptions with ultrahigh response time (<0.5 ms, 2 kHz) for restoration. The device covered with microhairs (50 μm diameter and 300 μm height, AR = 6, hexagonal layout, and ~4400/cm^2) exhibits mapping of electrical signals induced by noncontact airflow and identifying the direction, incident angle, and intensity of wind to the sensor. For potential applications, we implement the hairy electronics to a sailing robot and demonstrate changes in locomotion and speed by detecting the direction and intensity of airflow.

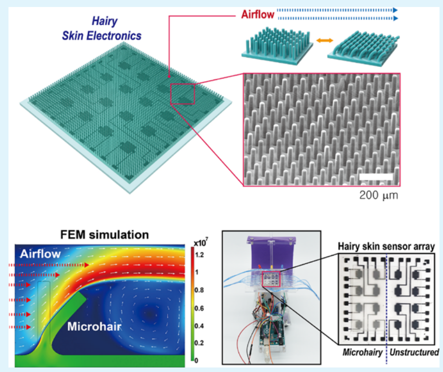

KEYWORDS: *E-skin, microhair, biosensor, flexible device, graphene*

INTRODUCTION

Investigations in the somatosensory system and the haptic perception of human skin have dramatically improved the performances of rubber-based medical sensors and synthetic electronic skins (E-skins).[1−3] Much effort has been made to mimic the structural and material features of sensory receptors of human skin.[4,5] Flexible and stretchable skin electronics have been designed to mimic human skin by introducing novel architectures with inorganic materials.[6−9] Inspired by the mechanoreceptors and thermoreceptors, E-skins have mostly been focused on pressure sensing or temperature sensing.[10−12] Beyond such applications, E-skins have evolved by stacking multiple layers into a device for multimodal sensing (e.g., pressure, strain, temperature, humidity, or chemicals).[11−13] Such devices are generally fabricated with carbon-based polymeric materials, metal particles, or hybrid composites on a polymeric substrate to ensure skin-like flexibility.[10,11,13−15] Despite excellent performances of detecting physical forces by contact, multimodal E-skins with high sensitivity to noncontact forces by convective airflow have rarely been reported. Several groups have demonstrated measurements of noncontact forces induced by human breath and airflow applied perpendicularly to the E-skin.[11,13,16] However, unlike real skin, which is covered with hair, such devices cannot trace the direction, incident angle, and intensity profile of the convective airflow.

In recent years, the employment of nano-/microscale structures inside the sensing layer or the outer surfaces of a device has been highlighted for improvements in the performances and functionalities of E-skins and physical sensors. For example, the interlocking of nanohairs or dome-like architectures were implemented into passive sensing layers to improve the sensitivity and responsiveness of sensor devices.[16,17] Micropatterns were also introduced on the top surface of skin-like electronics to mimic structures on a human fingerprint for effective detection of vibrations.[18] Moreover, microhair architectures on the bottom surface of such devices improved adaptability on nonflat skin, resulting in effective detection of amplified biosignals (e.g., ECG or pulsations) for in vitro diagnostics.[19−21] The stretchable strain sensors with three-dimensional (3D) hair structure can effectively detect

Received: January 29, 2019
Accepted: March 14, 2019
Published: March 14, 2019

DOI: 10.1021/acsami.9b01427
ACS Appl. Mater. Interfaces 2019, 11, 13608−13615

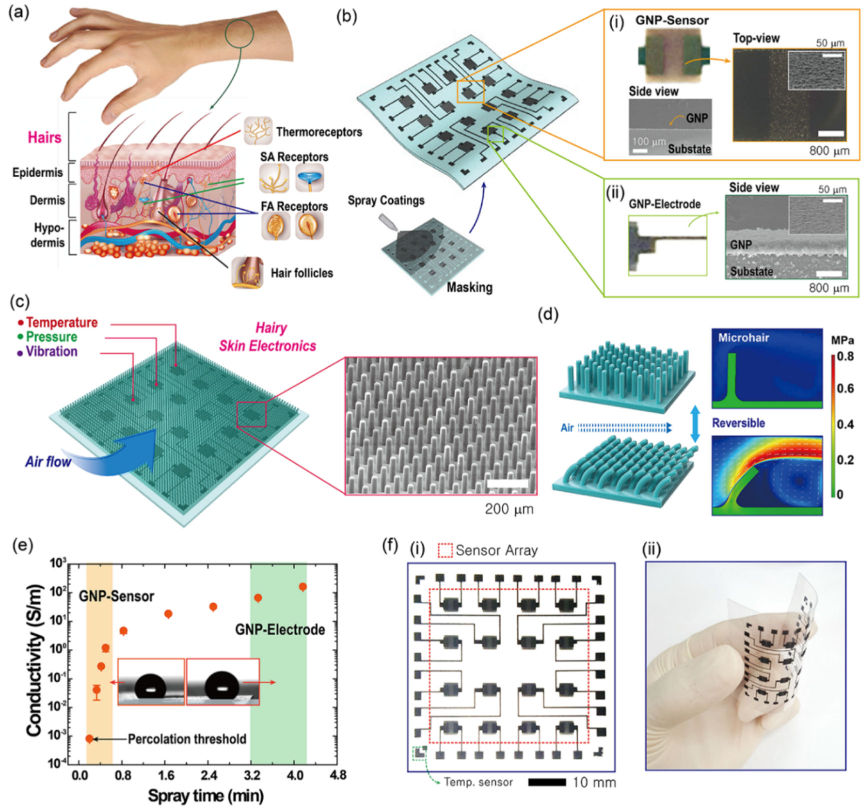

Figure 1. Hairy skin electronics with GNP sensor array. (a) Hairy skin of human with a variety of sensory receptors. (b) GNP sensor array and electrodes on a PEN substrate using the spray coating method through stencil masks. The images on the right show coating properties of the GNP-based sensor (0.4 min coating) and electrode (4.2 min coating) with top- and side-view SEM images. (c) Schematic design of the graphene-based sensor array densely populated with microhairs (~4400/cm^2). SEM image shows microhairs with 50 μm diameter and 300 μm height, AR = 6, on a hexagonal layout. (d) Schematic illustration and simulation results showing bending of PDMS microhairs by airflow. (e) Electrical conductivity of GNP films depending on spray coating time. The GNP sensor requires low conductivity to achieve high sensitivity for temperature and pressure (left orange block range), whereas the GNP electrode prefers high conductivity (right green block range). Insets show contact angles of water droplets for the GNP sensor film (125°) and the GNP electrode film (136°). (f) Photograph of the flexible GNP E-skin.

out-of-plane force.[22] Commonly found on the outer surface of animals, hairy structures have a critical role in effectively sensing ultralight touch or flow beyond skin. This is because the hairs with high aspect ratio (AR) connected to sensory organs can monitor displacements and vibrations. Bats, for instance, utilize hairs on their wings to recognize airflow patterns during flight.[23] Insects, using fine hairs arrayed throughout their bodies, can sensitively perceive the disturbance of airflow produced by approaching predators or toxic gases.[24] Sensors have commonly functioned using silicon-based microelectromechanical system technology to detect hair shaft displacements with rubber or microcantilever hair materials.[25,26] However, they are based on rigid substrates and require sophisticated fabrication techniques, which cannot be applied to soft E-skins or flexible wearable electronics. Thus, mimicking the hairy structures of skin remains unexploited but promising to develop multimodal E-skins capable of sensing various contact/noncontact forces and improve performances (e.g., sensitivity and fast response) for novel soft robotics, wearable devices, and medical applications.

To fabricate the percolation network as sensing elements in flexible skin electronics, various inorganic or organic nanoparticles have been used.[27,28] Among them, graphene-based nanoflakes are known to be solution-processable, cost effective for mass production, and have good mechanical and electrical properties.[29] In addition, they are relatively stable to thermal and electrical noises, showing high signal-to-noise ratio (SNR) of electrical output signals in response to thermal and mechanical stimuli.[30] By controlling the structural features and functional chemistries of graphene networks, graphene-based nanoparticles can also be applied as the sensing layer (e.g., pressure, temperature, or vibration).[31,32] Such structural network on a thin polymeric film has been demonstrated as flexible or stretchable electrodes because of excellent mechanical and electrical properties.[29,33]

In this work, we developed hairy skin electronics for multimodal detection inspired by hairs and sensory systems of the human skin. The array of sensors and electrodes are fabricated by a simple thermal spray coating process of graphene nanoplatelets (GNPs) onto a flexible substrate by changing the stencil masks. Our device with percolation networks of GNP sheets (5 × 5 cm^2, 16 pixels) can detect the spatial distribution of applied pressures with localized temperature differences, which is a behavior similar to the human skin. Microhairs employed on the electronics were capable of mapping electrical signals induced by noncontact airflow to identify the direction, incident angle, and intensity of the wind applied. Moreover, we integrated our hairy device with a sailing robot to control its movements by the direction and intensity of noncontact air-flows.

DOI: 10.1021/acsami.9b01427
ACS Appl. Mater. Interfaces 2019, 11, 13608−13615

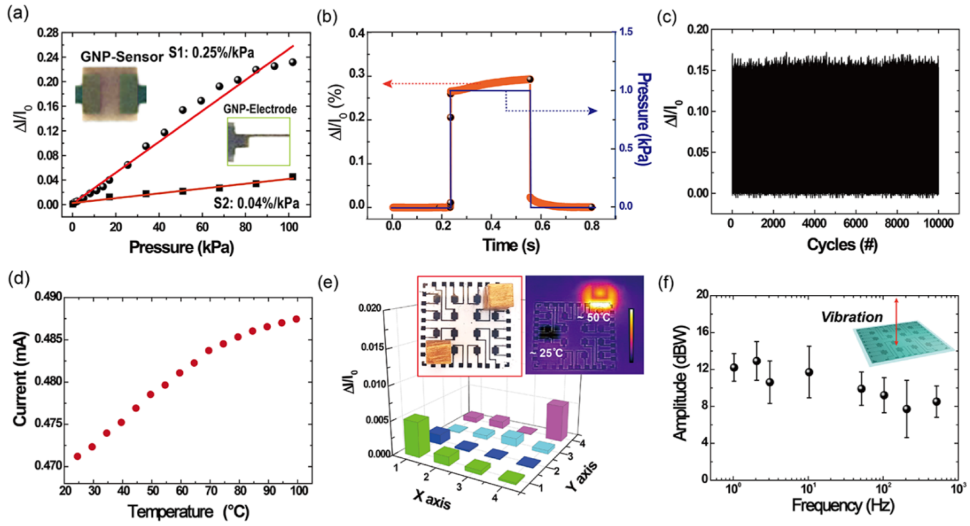

Figure 2. Electrical current responses induced by pressure and temperature changes. (a) Electrical responses represented by the rate of current change of the GNP sensor and electrode with static vertical pressures. (b) Response to current change for the GNP sensor under press-and-release operation. The estimated response time is as fast as 1 ms to deformation and 0.5 ms to restoration with applied pressure of 1 kPa. The accuracy of measurement is 0.5 ms. (c) Reproducible operation of the device. (d) Current responses of the GNP sensor depending on temperature changes from 25 to 100 °C. The temperature change step is 5 °C. (e) Thermal imaging and response profile of the sensor array with two weights of the same mass (~1.8 kPa) with different temperatures. Temperatures of top right and bottom left sensors are 50 °C (treated in hot baking oven) and 25 °C (RT), respectively. 3D response profiles to current changes of sensor array are driven from only pressures after temperature calibration. (f) Detection of vertical vibrations. The device shows frequency responses over 5 dB in SNR for vibrations ranging from 1 to 500 Hz. Inset shows vertical vibration measurement.

RESULTS AND DISCUSSION

Figure 1a shows hairy, human skin, the outermost organ of a human, composed of two layers: the protective epidermis and the dermis composed of multiple sensory systems. The dermis is occupied with cutaneous receptors which can sense various tactile stimuli (e.g., touch, pressure, vibration, heat, and pain). In particular, the thermoreceptors respond rapidly to absolute and relative changes in temperature, primarily within the innocuous thermal range below ~100 °C.[34] As shown in the inset images of Figure 1a, inside the dermis are also slow-adaptive (SA) mechanoreceptors which react to general pressure (0.1−100 kPa) and fast-adaptive (FA) mechanoreceptors which are activated by dynamic pressure and vibration (50−400 Hz).[35] Meanwhile, hairs connected to follicles can detect subtle structural displacements induced by airflow or ultralight touch above the skin. Inspired by the sensory systems of human skin and hairs on top, we developed an electronic device with a graphene-based sensor array and densely populated microhairs (~4400/cm^2), as shown in Figure 1c. The bottom GNP sensor array panel can simultaneously retrieve information on the pressure, temperature, and vibrations corresponding to the sensing range of human perceptions. When heat or loads are applied on specific areas, the sensor array (16 pixels) can map profiles of electrical change for pressure and temperature after calibration with the surrounding temperature. Here, the surrounding temperature is monitored with an additional temperature sensor located at the outside edge of our E-skin, as shown in Figure 1fi. In addition, we employed numerous microhairs (50 μm diameter and 300 μm height, AR = 6, hexagonal layout) to sense subtle mechanical displacements induced by convective airflow and detect the direction, incident angle, and intensity of the airflow (see Figure 1d).

To fabricate the sensor array (4 × 4 pixels) of our hairy electronics, we employed a facile method of thermal spray coating a GNP suspension over a large area (5 × 5 cm^2) of a flexible polyethylene naphthalate (PEN) substrate, as illustrated in Figure 1b and Supporting Methods section in the Supporting Information. For clear mapping signals, we separated regions of sensors and electrodes using different stencil masks. Here, the thickness of the GNP films for sensors and electrodes was controlled by changing the processing time of GNP suspension (~1.5 mg/mL) with constant flowrate (~8 mL/min). As shown in Figure 1b(i,ii),e, the GNP-based sensors and electrodes in the device have different structural features, density, and electrical conductivity. The regularly ordered GNP sensors were laminated on a PEN backbone with spray coating for 0.4 min (~0.3 S/m), resulting in low density of GNPs near the percolation threshold (Figure 1b(i)). The percolation networks, which acted as sensors (4 mm × 4 mm for each sensor, ~15 μm thickness), showed linear changes in electrical resistance with response to pressure or temperature (see Figure 2a,d). On the other hand, electrodes without cracks (~170 μm thickness), additionally coated with GNPs for 4.2 min, indicated low resistivity (~172 S/m) (see Figures 1b(ii) and S1) without significant changes in resistivity during bending tests (<0.052 mm^{-1}of bending curvature: see the Supporting Information, Figure S2). Here, contact resistance between the sensor and electrode is negligible because they are based on the same material. To minimalize noise effects caused by water molecules, the microstructured conductive patterns showed hydrophobicity with high contact angles (<120°) as shown in inset images of Figure 1e. Figure 1f shows the flexible E-skin with sensor and connector arrays fabricated by a simple solution process of GNP suspension.

In Figure 2a, the GNP-based sensor shows linear response to electrical current under applied pressures (0.1−102 kPa) (see the Supporting Methods section in the Supporting Information for detailed measurements). When pressure was applied to the sensor, the vertical strain increased electrical conductivity of

DOI: 10.1021/acsami.9b01427
ACS Appl. Mater. Interfaces 2019, 11, 13608−13615

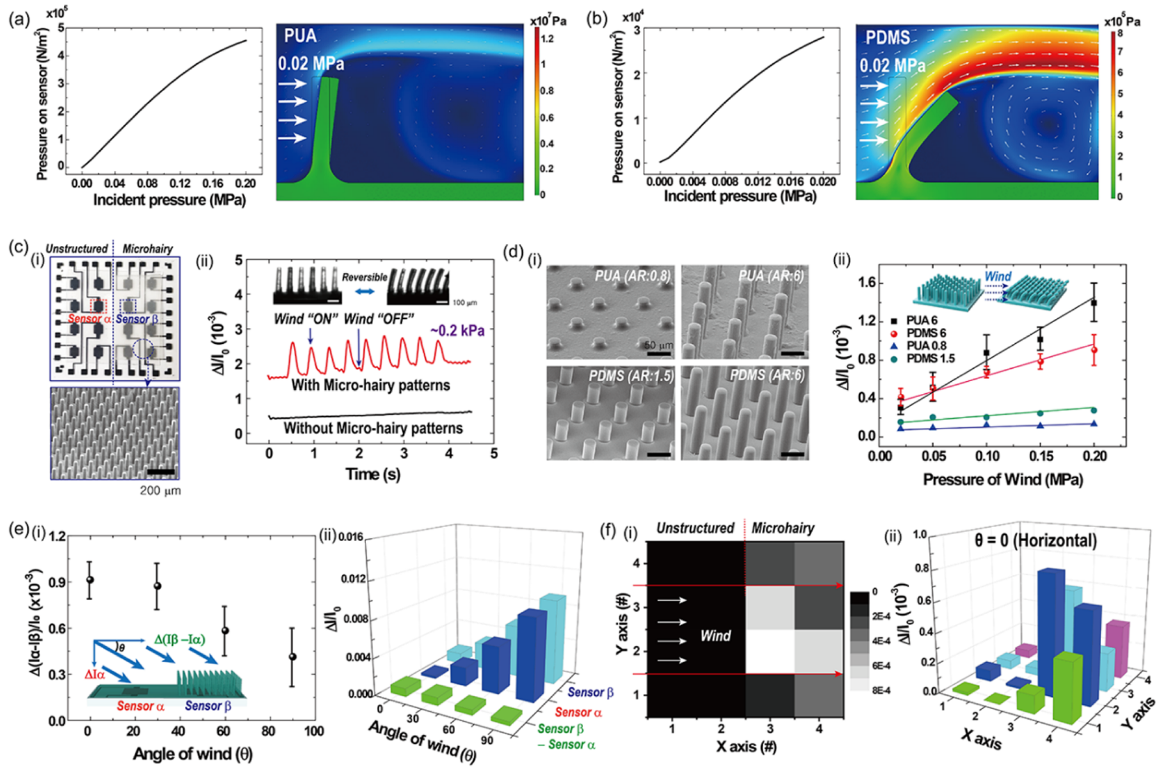

Figure 3. Sensitive detection of noncontact airflow. (a,b) FEM simulation results for PUA and PDMS microhairs. (c) Detection of convective airflow with the sensor array. (i) Optical images of the unstructured (left 8 pixels) and microhairy (right 8 pixels) graphene sensor array. SEM images below magnify the microhairs. (ii) On/off responses of current changes in airflow with and without microhairs. (d) Current changes of electronics depending on the intensity of wind regulated by the pressure of the air with (i) different materials and ARs of hairy structures. Inset in (ii) shows schematics indicating reversible bending of microhairs by airflow. (e) Detection of incident angle (θ) of the airflow. (i) Two sensors without (sensor α) and with (sensor β) microhairs were used to extract microhair contribution component (sensor α - sensor β). (ii) 3D profiles of electrical changes of sensor α, sensor β, and sensor α - sensor β. (f) Detection of airflow direction. (i) Air blown from left (unstructured) to right (microhairy) to the area where the two sensors in the middle are directly affected by the airflow. (ii) 3D sensor response profiles for airflow in horizontal direction (θ = 0) airflow.

the GNP percolation networks. Herein, physical contacts among conductive GNP sheets increased, whereas spatial vacancies reduced (see the Supporting Information and Figure S3 for detailed mechanism). Ultrafast response time (<0.5 ms) and low hysteresis from loading and unloading of applied pressure were observed due to the mechanism underlying reversible slippage and recovery of overlapping areas in the GNP-based architectures, as shown in Figure 2b. The GNP sensor showed high sensitivity ($S \approx 0.25\%$/kPa) in response to pressure, defined as $S = (\Delta I/I_0)/\Delta P$. Here, ΔI is the current change due to vertically applied pressure (ΔP). As the equation is defined as $y = ax + b$, where y is the current change rate ($\Delta I/I_0$), x is pressure (in kPa) or temperature (°C), a and b are the slope and y-axis intercept of current change rate versus pressure or temperature curves, respectively, the equation for pressure response is estimated as $y = 0.0025x + 0.0014$ (with R^2 = 0.98 for linearity) (see the Supporting Information Figure S4a). In addition, we observed highly reproducible signals over multiple cyclic tests (<10 000 cycles, 50 kPa) with stable dynamic behaviors of loading and unloading by utilizing a pressure controller with 1 Hz recording in Figure 2c (see the Supporting Information, Figure S5 for additional dynamic responses). The electrodes did not show significant changes in electrical current (~0.04%/kPa) because of applied pressures (0.1−102 kPa) and bending stress (<0.052/mm of bending curvature) because strong physical and electrical interaction among the GNPs with a high coating is relatively insensitive to externally mechanical deformations (see Figure 2a and the Supporting Information, Figure S2 and Supporting Methods section in the Supporting Information).[36]

To investigate temperature dependency of the GNP sensor, we recorded changes in electrical resistance as a function of applied temperature (see Supporting Methods section in the Supporting Information for detailed experimental setup). In Figure 2d and the Supporting Information, Figures S4b and S6, a linear response to various temperatures was observed; this can be explained by the widely accepted concept of variable range hopping charge-transport mechanism among the neighboring GNPs.[37] Monitoring surrounding temperature with the exterior temperature sensor, the device showed linear responses of pressure-dependent electrical signals under various temperatures (25−100 °C). Based on the data of Supporting Information, Figure S7, our E-skin with regularly-ordered sensors (16 pixels in 5 × 5 cm^2) can monitor spatial distributions of pressure discriminated from localized temperature differences. To demonstrate such behavior, two weights (18 g on 1 cm^2) with different temperatures (~50 °C top right and ~25 °C bottom left) were placed on two different locations of the sensors as shown in the upper images of Figure 2e. The resulting 3D intensity profiles of pressure and temperature are displayed in Figure 2e and the Supporting Information, Figure S8. As shown, the GNP-based E-skin can

DOI: 10.1021/acsami.9b01427
ACS Appl. Mater. Interfaces 2019, 11, 13608−13615

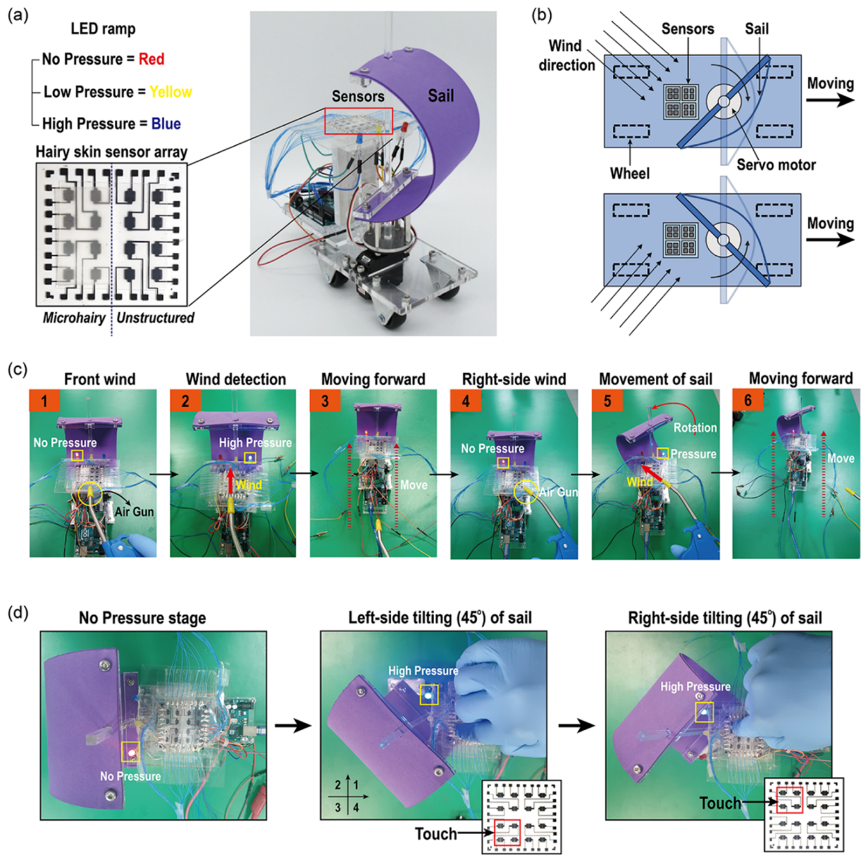

Figure 4. Operation of a sailing robot. (a) Sailing robot operation by detection of noncontact airflow. Left side of the array (8 pixels) is structured with PUA microhairs (50 μm diameter and 300 μm height, AR = 6, hexagonal layout, and ~4400/cm^2) and the right side (8 pixels) is not patterned. Intensity of wind is displayed as red (no pressure), yellow (low pressure), and blue (high pressure) LEDs. The sequential screenshots show the detection of intensity, direction of airflow, and the resulting sailing operations. (b) Schematic illustrations showing operating principle of the sailing robot depending on the direction of the wind. (c) Sequential screenshots show sensitive detection of intensity and direction of airflow and the resulting sailing operations. (d) Change in the direction of the sail in electrical responses to the physical touch pressure on the hairy device with sensor array.

detect the spatial distribution of pressure after calibration of data with localized temperature differences.

To sense vibration like the human skin (50−400 Hz), the device requires fast response time (<2.5 ms) to record minute electrical changes induced by physical contact.[2] Rigid fingerprint-like textures are applied to amplify vibrational signals transferred into the soft dermis layer.[38] In our investigation, the porous GNP layer provided ultrafast and reversible responses (<0.5 ms) as shown in Figure 2b for vibrational stimuli up to 2 kHz without critical signal loss. Here, the GNP sensor can detect vibrations in wide ranges (1−500 Hz) with high SNR values (>5 dB) (see Figure 2f); this range is similar to that of human perceptions detected by the FA mechanoreceptors. To amplify vibrations of friction induced by physical contact, we additionally employed polyethylene terephthalate (PET) microlines (300 μm width, 70 μm height, and 300 μm spacing distance) on the top surface of the sensor array, as shown in Figure S8a. Two surfaces with different textures (flat and microlines of PET: see SEM below images of Figure S9a) were then laminated on the top of the microlined sensor with a loading pressure of ~42 kPa and repeatedly rubbed back and forth with constant velocity of ~7 mm/s (see the Supporting Methods section in the Supporting Information for details). Unlike the flat surface, the line-textured surface monitored hierarchical sinusoidal waveforms as shown in the Supporting Information, Figure S9b. Specifically, the number of hierarchical, periodic peaks in the Supporting Information, Figure S9c matched accurately with the number of ridges on the textured surface because of physical interactions between the device and the engaged surface. By attaching to the volunteer's neck, the electronic device was able to monitor tiny vibrations of voices of a word ("Hello") and a sentence ("I am good man") (see the Supporting Methods section and Figure S10 in the Supporting Information). Moreover, waveforms of pulsations were obtained by attaching the sensor onto the volunteer's wrist (see the Supporting Information, Figure S11).

The detection capability of the microhairs on the electronics is described in Figure 3. Finite element method (FEM) simulation was first performed to understand the mechanical deformation of microhairs and their vibrations (or pressure) transferred to the GNP film, resulting from the airflow (Figure 3a,b and Supporting Methods section in the Supporting Information and Supporting Videos 1,2). Poly(urethane acrylate) (PUA) (Young's modulus: 19.8 MPa) and poly(dimethylsiloxane) (PDMS) (Young's modulus: 2 MPa) microhairs were compared to test the influence of material properties on their bending against continuous airflow. The graphs of Figure 3a,b show incident pressure (0−0.2 MPa for PUA and 0−0.02 MPa for PDMS) against Von Mises stresses applied on the hair device when the forces of airflow and pillar deformation reach equilibrium. The PDMS hairs displayed higher bendability than the PUA hairs against airflow because

DOI: 10.1021/acsami.9b01427
ACS Appl. Mater. Interfaces 2019, 11, 13608−13615

of low Young's modulus but low delivery of pressure onto the GNP film sensor, owing to their low bending stress. Screenshots of the FEM results show moments when the PUA and PDMS micropillars are subjected by the airflows of 0.02 MPa. The colored bars indicate degrees of pressure transferred onto the GNP film by the bending of micropillars.

In Figure 3ci, we developed hairy skin electronics (16 pixels) by laminating the microhair structures (50 μm diameter and 300 μm height, AR = 6, hexagonal layout, and ~4400/cm^2) on the right side of the GNP-based sensor array (8 pixels) to detect convective airflow (see the Supporting Information, Figure S12 for fabrication of microhair structures). The optical images in insets of (Figure 3cii) show reversible displacement of high-AR microhairs by flowing air/gas in the horizontal direction. By switching airflow on/off (~0.2 kPa, 9 times) onto the sensors with microhairs, we demonstrated on/off responses of current changes with airflow, whereas the sensor without microstructures rarely activated, as shown in Figure 3cii). Effects on electrical responses with different materials and ARs of hairy structures (see SEM images of Figure 3di) were investigated. In our measurements, the sensors mostly showed linear changes in electrical responses to the pressure generated by the horizontal airflow, $(\Delta I/I_0)/\Delta P$. The reversible displacements of microhairs by airflow in the shear direction play a key role in transmitting electrical signals to the device, allowing the microhairs of high AR to attain higher sensitivity than those of lower AR (Figure 3dii). The PDMS microhairs showed greater electrical responses than PUA microhairs against wind pressure below 0.05 MPa, owing to the high bendability of PDMS. However, the larger bending stress of PUA microhairs generates larger responses against wind pressure. Our device showed high sensitivity and fast response time (<500 μs), so that minimum detectable wind pressure is ~0.12 Pa for PUA and ~0.08 Pa for PDMS per single microhair.

In addition, the hairy E-skin can perceive the incident angle (°) of airflow while monitoring electrical signals of sensors α and β at the same time (see the inset illustration of Figure 3e(i)). The PUA microhairs are solely used due to high-efficient transfer of pressures on the device. Based on the beam bending theory,[39] the degree of microhair displacement is affected by the incident angle of airflow. Thus, electrical changes, $\Delta(I_\alpha - I_\beta)/I_0$, from different displacements of microhairs can be estimated in Figure 3ei. Herein, I_α and I_β are the electrical signals of sensor α and sensor β, respectively. Sensor α, which does not have microhairs, monitors the vertical stress; sensor β, which has microhairs, measures the horizontal stress. Figure 3eii shows the 3D profiles for electrical changes of sensor α, sensor β, and difference between sensors α and β. To detect the direction of applied airflow, we obtained 2D and 3D profiles mapping electrical signals of the hairy sensor array for applied airflow from the left in a horizontal direction (θ = 0), as shown in Figure 3fi,ii). In addition, 3D spatial distribution of electrical changes in response to oblique airflow (θ = 60) is displayed in the Supporting Information, Figure S13. Here, the intensity of electrical change decreases as the wind reaches the edges of the microhairs because of scattering of convective forces.

Further optimizations of our flexible electronic device with microhairs may potentially bring forth applications beyond advanced medical devices or E-skins, to prosthetic skins or robotics through its high detection of airflows and physical touches. In order to demonstrate such capabilities, we attached our hairy device onto a sailing robot to control its movement by perceiving noncontact airflow (see the Supporting Information, Figure S14). The sailing robot moves only by the airflow without any additional power. To effectively detect the intensity and direction of airflow, the left side of the sensor array (8 pixels) is microstructured with PUA microhairs (50 μm diameter and 300 μm height, AR = 6, hexagonal layout, and ~4400/cm^2), whereas the right side (8 pixels) is not patterned (see Figure 4a and Supporting Methods section in the Supporting Information). The intensity of wind pressure can be distinguished as no pressure, low pressure (<0.04 MPa wind pressure), and high pressure (>0.04 MPa wind pressure), which are displayed by light emitting diodes (LEDs) of different colors (red, yellow, and blue respectively). As shown in Figure 4b, the sailing robot harnessed only wind as the power source to move forward. The area of the sail on which force of the blowing wind was applied varied depending on the direction of the sail. The sail must be as perpendicular as possible to the direction of the blowing wind to obtain maximum work from the wind. Moving direction of the sailing robot is always the front because of the fixed wheels. Figure 4c presents the automatic control of sail direction using the hairy sensor integrated on the sailing robot (Supporting Video 3). An airflow of high pressure was first applied to the front of the hairy device (screenshot 1). The device with microhairs detected the airflow (screenshot 2) and allowed the sailing robot to move straight toward the airflow (screenshot 3). An in-plane airflow of 45° was then applied from the right bottom to left top (screenshot 4). The device with microhairs detected the angle of airflow, changed the sail angle to the direction of the airflow, and moved the sailing robot toward the applied airflow (screenshot 5). We also demonstrated changes in the direction of the sail with electrical responses to pressures of physical touches onto the hairy electronics, as shown in Figure 4d and Supporting Video 4. The directions were divided into four quadrants: if one of the four individual sensors belonging to each quadrant was touched, the sail tilted 45° in the direction of the touched sensor. Movements of the sail to the second or third quadrant were successfully demonstrated with response to high-pressure touch (~15 kPa), which corresponds to the pressure of a general touch in human tactile perception.

CONCLUSIONS

We present a design for flexible multifunctional skin electronics, which detect various tactile stimuli of temperature, pressure, and vibration in the general range of human tactile perception. The sensors and connectors in the device were fabricated through a simple spray coating method of GNPs. The sensor array within the device (16 pixels) is highly sensitive, monitoring electrical change profiles of pressure and temperature. We developed microhairs to detect minute displacements induced by the convective airflow above the device. By monitoring stresses applied to the arrayed sensors, we obtained 3D profiles with spatial distribution to estimate the directions, incident angles, and intensity of applied airflows. To demonstrate potentials of our device beyond E-skins and smart medical systems, we attached the device onto a sailing robot and detected the noncontact airflow to control its movement and the direction of the sail.

EXPERIMENTAL METHODS

Fabrication of GNP Sensor Array. The GNP sensor array and electrodes within the E-skin were fabricated through a spray coating method of GNP suspension using stencil masks. First, the patterned

DOI: 10.1021/acsami.9b01427
ACS Appl. Mater. Interfaces 2019, 11, 13608−13615

sensor array (4 × 4 pixels) was formed on a PEN substrate with specific spray coating time (30 s; flowrate of 8 mL/min) of the GNP suspension (1.5 mg/mL) on a hot plate (85 °C) using the 1st stencil mask, followed by thermal baking (120 °C) to dry the solution for 10 min. After an appropriate alignment between the align marks of the GNP film formed on the PEN and the 2nd stencil mask, the electrodes were formed on both sides of the sensor array with specific spray coating time (250 s; flowrate of 8 mL/min) of the GNP suspension (1.5 mg/mL) on a hot plate (85 °C), followed by thermal baking (120 °C) to dry the solution for 30 min. The graphene sensor array was finally completed by assembling the thin PEN protecting layer onto the GNP films to prevent the GNP particles from escaping when pressure and vibration are applied or released.

Fabrication of Micropatterns. To fabricate the microline pattern ridges, SU-8 photoresist was used for conventional lithographic patterning by spin coating (3000 rpm) and two-step curing processes (65 °C for 3 min; 95 °C for 9 min). After reactive ion etching with 30 sccm of CH_4 gas and 150 W of plasma power, the completed ridge structures were obtained as a periodic structure with line width, height, and spacing of 300, 70, and 300 μm, respectively; these specifications are similar to those of human fingerprint structures. To design the microhairs, a PDMS mold (Sylgard 184, DOW Corning) was first replicated from a silicon master mold. A 10:1 elastomer-to-crosslinker ratio of PDMS mixture (Sylgard 184, Dow Corning) was then used, followed by stirring for 1 h. The mixture was poured on the silicon master and subjected to vortex mixing (30 min) followed by sonication (1 h). A vacuum desiccator was used to degas the PDMS mixture for 2 h. After the PDMS mixture was thermally cured at 85 °C in a baking oven, the PDMS master was completed. A prepolymer PUA (PUA MINS 311 RM) was then dispensed onto the PDMS master. Finally, the replicated PUA mold was detached from the PDMS mold with periodic microhair patterns of distinct diameters (50, 100, and 300 μm), heights (100, 250, and 300 μm), and spacings (100 and 300 μm).

Noncontact Wind Force Measurements. Wind forces were applied on the microhairs of the device using an air gun in the horizontal direction. The wind generates shear force by bending the microhairs, inducing pressure onto the GNP film sensor. Intensity of the wind was regulated by controlling the pressure of air from the blow gun. To detect dependency on incident angles for electrical responses by airflow, responses of two sensors (sensor β with microhairs and sensor α without microhairs) were measured for specific incident angles (0, 30, 60, and 90°) at the same time. The responses by the shear force because of displacements of microhairs were then calculated by difference between sensors α and β (sensor α − sensor β). For detection of airflow direction, the right side of the array (8 pixels) is microstructured with microhairs (50 μm diameter and 300 μm height, AR = 6, hexagonal layout, and ~4400/cm^2) and the left side is not patterned. Wind is blown from left (unstructured) to right (microstructured) with specific incident angles (θ = 0 or 60) and subjected to the central area with two lines which is located in the middle of the sensor array.

■ ASSOCIATED CONTENT

Supporting Information

The Supporting Information is available free of charge on the ACS Publications website at DOI: 10.1021/acsami.9b01427.

Preparation of GNP suspension, fabrication of graphene sensor array, fabrication of microline pattern ridges, fabrication of microhair structures, electromechanical measurements of the E-skin with GNP-based sensor array, temperature measurements, pressure-sensing properties on temperature variations, FEM simulation, measurements of interacting vibration by rubbing contact, noncontact wind force measurements, contact angle measurements, sheet resistance measurements, a sailing robot, schematic illustration of sensor fabrication, GNP film cracks, response in bending curvature, operating mechanism of sensor, dynamic sensor responses, current versus temperature curve, sensor pressure responses with temperature calibration, 3D response profile of sensor responses, vibration responses, detection of voice vibration, pulse measurements, sensor response of oblique airflow, a sailing robot (PDF)

FEM simulation, simulation of PDMS bending by wind (AVI)

FEM simulation, simulation of PUA bending by wind (AVI)

Sailing robot operation by airflow (AVI)

Sailing robot operation by finger touch (AVI)

■ AUTHOR INFORMATION

Corresponding Author

*E-mail: chpang@skku.edu..

ORCID

Changsoon Choi: 0000-0003-4456-4548

Changhyun Pang: 0000-0001-8339-7880

Author Contributions

S.C. and C.P. conceived this work. S.C., W.S., and C.C. designed and fabricated the E-skin devices. S.C., H.M., and H.J.L. analyzed the properties and electrical signals of the devices. J.K. and C.P. conducted FEM simulation. D.K., C.K., and J.K. fabricated the sailing robot and measured the sailing operations. S.C. and C.P. analyzed the data and wrote the paper. All authors reviewed the manuscript and provided feedback.

Notes

The authors declare no competing financial interest.

■ ACKNOWLEDGMENTS

This work was supported by the Basic Science Research Program (NRF-2018R1A6A3A01011866) through the National Research Foundation of Korea funded by the Ministry of Education. We gratefully acknowledge support from the National Research Foundation of Korea (NRF-2019R1C1C1008730). This study has been conducted with the support of the Korea Institute of Industrial Technology (KITECH JA-19-0001), and Gyeongi-Do Technology Development Program (KITECH IZ-19-0003) for the "Development of smart textronic products based on electronic fibers and textiles".

■ REFERENCES

(1) Boutry, C. M.; Negre, M.; Jorda, M.; Vardoulis, O.; Chortos, A.; Khatib, O.; Bao, Z. A Hierarchically Patterned, Bioinspired E-Skin Able to Detect The Direction of Applied Pressure for Robotics. *Sci. Robot.* **2018**, *3*, No. eaau6914.

(2) Chortos, A.; Liu, J.; Bao, Z. Pursuing Prosthetic Electronic Skin. *Nat. Mater.* **2016**, *15*, 937−950.

(3) Wang, S.; Xu, J.; Wang, W.; Wang, G.-J. N.; Rastak, R.; Molina-Lopez, F.; Chung, J. W.; Niu, S.; Feig, V. R.; Lopez, J.; Lei, T.; Kwon, S.-K.; Kim, Y.; Foudeh, A. M.; Ehrlich, A.; Gasperini, A.; Yun, Y.; Murmann, B.; Tok, J. B.-H.; Bao, Z. Skin Electronics from Scalable Fabrication of An Intrinsically Stretchable Transistor Array. *Nature* **2018**, *555*, 83−88.

(4) Wan, C.; Chen, G.; Fu, Y.; Wang, M.; Matsuhisa, N.; Pan, S.; Pan, L.; Yang, H.; Wan, Q.; Zhu, L.; Chen, X. An Artificial Sensory Neuron with Tactile Perceptual Learning. *Adv. Mater.* **2018**, *30*, 1801291.

(5) Tee, B. C. K.; Chortos, A.; Berndt, A.; Nguyen, A. K.; Tom, A.; McGuire, A.; Lin, Z. C.; Tien, K.; Bae, W.-G.; Wang, H.; Mei, P.;

DOI: 10.1021/acsami.9b01427
ACS Appl. Mater. Interfaces 2019, 11, 13608−13615

Chou, H.-H.; Cui, B.; Deisseroth, K.; Ng, T. N.; Bao, Z. A Skin-Inspired Organic Digital Mechanoreceptor. *Science* **2015**, *350*, 313−316.
(6) Kim, D.-H.; Lu, N.; Ma, R.; Kim, Y.-S.; Kim, R.-H.; Wang, S.; Wu, J.; Won, S. M.; Tao, H.; Islam, A.; Yu, K. J.; Kim, T.-i.; Chowdhury, R.; Ying, M.; Xu, L.; Li, M.; Chung, H.-J.; Keum, H.; McCormick, M.; Liu, P.; Zhang, Y.-W.; Omenetto, F. G.; Huang, Y.; Coleman, T.; Rogers, J. A. Epidermal Electronics. *Science* **2011**, *333*, 838−843.
(7) Jang, K. I.; Chung, H. U.; Xu, S.; Lee, C. H.; Luan, H.; Jeong, J.; Cheng, H.; Kim, G. T.; Han, S. Y.; Lee, J. W.; Kim, J.; Cho, M.; Miao, F.; Yang, Y.; Jung, H. N.; Flavin, M.; Liu, H.; Kong, G. W.; Yu, K. J.; Rhee, S. I.; Chung, J.; Kim, B.; Kwak, J. W.; Yun, M. H.; Kim, J. Y.; Song, Y. M.; Paik, U.; Zhang, Y.; Huang, Y.; Rogers, J. A. Soft Network Composite Materials with Deterministic and Bio-Inspired Designs. *Nat. Commun.* **2015**, *6*, 6566.
(8) Kim, J.; Lee, M.; Shim, H. J.; Ghaffari, R.; Cho, H. R.; Son, D.; Jung, Y. H.; Soh, M.; Choi, C.; Jung, S.; Chu, K.; Jeon, D.; Lee, S. T.; Kim, J. H.; Choi, S. H.; Hyeon, T.; Kim, D. H. Stretchable Silicon Nanoribbon Electronics for Skin Prosthesis. *Nat. Commun.* **2014**, *5*, 5747.
(9) Zhang, Y.; Huang, Y.; Rogers, J. A. Mechanics of Stretchable Batteries and Supercapacitors. *Curr. Opin. Solid State Mater. Sci.* **2015**, *19*, 190−199.
(10) Bae, G. Y.; Pak, S. W.; Kim, D.; Lee, G.; Kim, D. H.; Chung, Y.; Cho, K. Linearly and Highly Pressure-Sensitive Electron Skin based on A Bioinspired Hierarchical Structural Array. *Adv. Mater.* **2016**, *28*, 5300−5306.
(11) Ho, D. H.; Sun, Q.; Kim, S. Y.; Han, J. T.; Kim, D. H.; Cho, J. H. Stretchable and Multimodal All Graphene Electronic Skin. *Adv. Mater.* **2016**, *28*, 2601−2608.
(12) Trung, T. Q.; Ramasundaram, S.; Hwang, B.-U.; Lee, N.-E. An All-Elastomeric Transparent and Stretchable Temperature Sensor for Body-Attachable Wearable Electronics. *Adv. Mater.* **2016**, *28*, 502−509.
(13) Park, J.; Kim, M.; Lee, Y.; Lee, H. S.; Ko, H. Fingertip Skin-Inspired Microstructured Ferroelectric Skins Discriminate Static/Dynamic Pressure and Temperature Stimuli. *Sci. Adv.* **2015**, *1*, No. e1500661.
(14) Lipomi, D. J.; Vosgueritchian, M.; Tee, B. C.-K.; Hellstrom, S. L.; Lee, J. A.; Fox, C. H.; Bao, Z. Skin-Like Pressure and Strain Sensors based on Transparent Elastic Films of Carbon Nanotubes. *Nat. Mater.* **2011**, *6*, 788−792.
(15) Gong, S.; Schwalb, W.; Wang, Y.; Chen, Y.; Tang, Y.; Si, J.; Shirinzadeh, B.; Cheng, W. A Wearable and Highly Sensitive Pressure Sensor with Ultrathin Glod Nanowires. *Nat. Commun.* **2014**, *5*, 3132.
(16) Park, J.; Lee, Y.; Hong, J.; Ha, M.; Jung, Y.-D.; Lim, H.; Kim, S. Y.; Ko, H. Giant Tunneling Piezoresistance of Composite Elastomers with Interlocked Microdome Arrays for Ultrasensitive and Multimodal Electronic Skins. *ACS Nano* **2014**, *8*, 4689−4697.
(17) Pang, C.; Lee, G.-Y.; Kim, T.-i.; Kim, S. M.; Kim, H. N.; Ahn, S.-H.; Suh, K.-Y. A Flexible and Highly Sensitive Strain-Gauge Sensor using Reversible Interlocking of Nanofibers. *Nat. Mater.* **2012**, *11*, 795−801.
(18) Chun, S.; Hwang, I.; Son, W.; Chang, J.-H.; Park, W. Recognition, Classification, and Prediction of The Tactile Sense. *Nanoscale* **2018**, *10*, 10545−10553.
(19) Pang, C.; Koo, J. H.; Nguyen, A.; Caves, J. M.; Kim, M.-G.; Chortos, A.; Kim, K.; Wang, P. J.; Tok, J. B.-H.; Bao, Z. Highly Skin-Conformal Microhairy Sensor for Pulse Signal Amplification. *Adv. Mater.* **2015**, *27*, 634−640.
(20) Baik, S.; Kim, J.; Lee, H. J.; Lee, T. H.; Pang, C. Highly Adapatable and Biocompatible Octopus-Like Adhesive Patches with Meniscus-Controlled Unfoldable 3D Microtips for Underwater Surface and Hairy Skin. *Adv. Sci.* **2018**, *5*, 1800100.
(21) Park, Y.; Shim, J.; Jeong, S.; Yi, G.-R.; Chae, H.; Bae, J. W.; Kim, S. O.; Pang, C. Microtopography-Guided Conductive Patterns of Liquid-Driven Graphene Nanoplatlet Networks for Stretchable and Skin-Conformal Sensor Array. *Adv. Mater.* **2017**, *29*, 1606453.
(22) Liu, Z.; Qi, D.; Leow, W. R.; Yu, J.; Xiloyannnis, M.; Cappello, L.; Liu, Y.; Zhu, B.; Jiang, Y.; Chen, G.; Masia, L.; Liedberg, B.; Chen, X. 3D-Structured Stretchable Strain Sensors for Out-of-Plane Force Detection. *Adv. Mater.* **2018**, *30*, 1707285.
(23) Sterbing-D'Angelo, S.; Chadha, M.; Chiu, C.; Falk, B.; Xian, W.; Barcelo, J.; Zook, J. M.; Moss, C. F. Bat Wing Sensors Support Flight Control. *Proc. Natl. Acad. Sci. U.S.A.* **2011**, *108*, 11291−11296.
(24) Han, H.; Baik, S.; Xu, B.; Seo, J.; Lee, S.; Shin, S.; Lee, J.; Koo, J. H.; Mei, Y.; Pang, C.; Lee, T. Bioinspired Geometry-Switchable Janus Nanofibers for Eye-Readable H_2 Sensors. *Adv. Funct. Mater.* **2017**, *27*, 1701618.
(25) Krijnen, G. J. M.; Dijkstra, M.; Baar, J. J. v.; Shankar, S. S.; Kuipers, W. J.; Boer, R. J. H. d.; Altpeter, D.; Lammerink, T. S. J.; Wiegerink, R. MEMs based Hair Flow-Sensors as Model Systems for Acoustic Perception Studies. *Nanotechnology* **2006**, *17*, S84−S89.
(26) Peleshanko, S.; Julian, M. D.; Ornatska, M.; McConney, M. E.; LeMieux, M. C.; Chen, N.; Tucker, C.; Yang, Y.; Liu, C.; Humphrey, J. A. C.; Tsukruk, V. V. Hydrogel-Encapsulated Microfabricated Haircells Mimicking Fish Cupula Neuromast. *Adv. Mater.* **2007**, *19*, 2903−2909.
(27) Hammock, M. L.; Chortos, A.; Tee, B. C.-K.; Tok, J. B.-H.; Bao, Z. 25th Anniversary Article: The Evolution of Electronic Skin (E-Skin): A Brief History, Design Consideration, and Recent Progress. *Adv. Mater.* **2013**, *25*, 5997−6038.
(28) Yeo, S. Y.; Park, S.; Yi, Y. J.; Kim, D. H.; Lim, J. A. Highly Sensitive Flexible Pressure Sensors based on Printed Organic Transistors with Centro-Apically Self-Organized Organic Semiconductor Microstructures. *ACS Appl. Mater. Interfaces* **2017**, *9*, 42996−43003.
(29) Zhu, Y.; Murali, S.; Cai, W.; Li, X.; Suk, J. W.; Potts, J. R.; Ruoff, R. S. Graphene and Graphene Oxide: Synthesis, Properties, and Applications. *Adv. Mater.* **2010**, *22*, 3906−3924.
(30) Balandin, A. A. Low-Frequency 1/f Noise in Graphene Devices. *Nat. Nanotechnol.* **2013**, *8*, 549−555.
(31) Yan, C.; Wang, J.; Lee, P. S. Stretchable Graphene Thermistor with Tunable Thermal Index. *ACS Nano* **2015**, *9*, 2130−2137.
(32) Chun, S.; Hong, A.; Choi, Y.; Ha, C.; Park, W. A Tactile Sensor using A Conductive Graphene-Sponge Composite. *Nanoscale* **2016**, *8*, 9185−9192.
(33) Chun, S.; Choi, Y.; Park, W. All-Graphene Strain Sensor on Soft Substrate. *Carbon* **2017**, *116*, 753−759.
(34) Schepers, R. J.; Ringkamp, M. Thermoreceptors and Thermosensitive Afferents. *Neurosci. Biobehav. Rev.* **2010**, *34*, 177−184.
(35) Zimmerman, A.; Bai, L.; Ginty, D. D. The Gentle Touch Receptors of Mammalian Skin. *Science* **2014**, *346*, 950−954.
(36) Hempel, M.; Nezich, D.; Kong, J.; Hofmann, M. A Novel Class of Strain Gauges based on Layered Percolative Films of 2D Materials. *Nano Lett.* **2012**, *12*, 5714−5718.
(37) Gómez-Navarro, C.; Weitz, R. T.; Bittner, A. M.; Scolari, M.; Mews, A.; Burghard, M.; Kern, K. Electroic Transport Properties of Individual Chemically Reduced Graphene Oxide Sheets. *Nano Lett.* **2007**, *7*, 3499−3503.
(38) Scheibert, J.; Leurent, S.; Prevost, A.; Debregeas, G. The Role of Fingerprints in The Coding of Tactile Information Probed with A Biomimetic Sensor. *Science* **2009**, *323*, 1503−1506.
(39) Nouira, H.; Foltête, E.; Hirsinger, L.; Ballandras, S. Investigation of The Effects of Air on The Dynamic Behavior of A Small Cantilever Beam. *J. Sound Vib.* **2007**, *305*, 243−260.

DOI: 10.1021/acsami.9b01427
ACS Appl. Mater. Interfaces 2019, 11, 13608−13615